




Suppression of intermediate antiferroelectric phase in sub-micron grain size $\text{Na}_{0.5}\text{Bi}_{0.5}\text{TiO}_3$ ceramics

L. Venkidu¹, D. E. Jain Ruth², M. Veera Gajendra Babu¹, P. Esther Rubavathi¹,
D. Dhayanithi³, N. V. Giridharan³, and B. Sundarakannan^{1,*} 

¹Department of Physics, Manonmaniam Sundaranar University, Abishekapatti, Tirunelveli, Tamil Nadu 627012, India

²Department of Physics, St. Xavier's College (Autonomous) Palayamkottai, Palayamkottai, Tamil Nadu 627002, India

³Department of Physics, Advanced Functional Materials Laboratory, National Institute of Technology, Tiruchirappalli 620015, India

Received: 17 June 2022

Accepted: 22 September 2022

Published online:

7 October 2022

© The Author(s), under exclusive licence to Springer Science+Business Media, LLC, part of Springer Nature 2022

ABSTRACT

Lead-free NBT ceramics with average grain sizes ranging from sub-micron (0.38 μm), micron (1.23 μm) and large-micron (3.65 μm) were prepared and the influence of grain size on structural, dielectric and ferroelectric properties are discussed in the present work. The effect of grain size on the intrinsic properties such as octahedral tilting, bond length, bond angle, octahedral distortion, crystallite size, lattice strain and lattice parameters were measured. Herein, the structural and the morphological properties at different sintering times were in direct congruence with the temperature-dependent dielectric and ferroelectric response of pure NBT ceramics and an intermediate antiferroelectric (AFE) phase suppressed in sub-micron NBT. This unusual feature of sub-micron NBT was thoroughly studied and distinguished from large-grain NBT ceramics. Based on the temperature-dependent P–E loops the maximum adiabatic change in temperature $\Delta T_{max} = -0.81$ K was obtained at the field strength of 55 kV/cm in micron NBT. Further, the large energy storage density of about $W_{rec} = 0.55$ J/cm³ was achieved by AFE phase transition in micron NBT through P–E loop data. Because of the coexistence of electro-caloric effect (ECE) and energy storage properties, the micron NBT was found to be the optimum grain size corresponding to the best dielectric and ferroelectric properties and therefore this porous-free NBT was suitable for application in functional devices.

1 Introduction

The ongoing miniaturization of electronic devices imposes a stringent requirement on lead-free ferroelectric materials and the properties of which are strongly influenced by the grain size dependence on

structural, dielectric, ferroelectric and piezoelectric were reported for their application in the field of energy storage devices, refrigeration and microelectronics [1, 2]. The dependence of grain size on electrical behavior, oxide-ion conduction, mixed ion electronic conduction, insulating and dielectric

Address correspondence to E-mail: sundarakannan@msuniv.ac.in

properties has been explained based on various defect mechanics in ferroelectric materials [2]. It is generally found that the grain size plays a consistent role in determining the dielectric permittivity despite the different powder processing and sintering methods such as spark plasma sintering [3], hot-pressing [3], conventional solid-state reaction [6], and two step-sintering [4] are employed. Major controversy related to the behavior of structural and dielectric properties in sub-micron to the coarse grain size samples is still desired to be revealed. Average grain size play an important role in the stabilization of crystal systems such as reported for BaTiO₃ (BT), Na_{0.4}K_{0.1}Bi_{0.5}TiO₃ (NKBT), NaNbO₃ (NN), Pb(Zr, Ti)O₃ (PZT) and Na_{0.5}Bi_{0.5}TiO₃ (NBT) [2, 5–7, 19]. In the case of BT, the cubic (*Pm-3m*) to tetragonal (*P4mm*) phase transition is suppressed due to decreasing grain size [2]. Kamel and With have reported an optimized poling field for improving dielectric and piezoelectric properties of PZT with different grain sizes [7]. The NaNbO₃-based nano and sub-micron samples clearly reported the suppression of antiferroelectric phase transition [5]. The maximum value of the dielectric and the piezoelectric constants are typically associated with the grain size in the range from 1 to 2 μm [3, 8].

Recently, researchers have focussed attention on NBT-based lead-free piezoelectric materials [1, 9] including its solid solutions with A-site [10], B-site [11] and A, B-sites [12] substitutions. NBT-based ferroelectrics have been more extensively studied due to rhombohedral symmetry [1], large P_r (38 μC/cm²) [9] and high T_m (320 °C) [12]. Because of the heterovalent ions at A-site (Na⁺/Bi³⁺), NBT has a disordered structure originating from the degree of probability associated with the occupation of the A-site by the Bi³⁺ and Na⁺ [9]. At room temperature NBT possess a rhombohedral distortion due to the hybridization of Bi (*6s²*) and O (*2p*) electrons, this distortion develops spontaneous polarization and therefore offers high ferroelectric and piezoelectric properties in NBT ceramics [9, 10]. The X-ray diffraction and dielectric studies of micron and coarse (large-micron) grain sizes revealed that pure NBT undergoes two structural phase transitions: first from rhombohedral (*R3c*) ferroelectric phase to tetragonal antiferroelectric (*P4bm*) phase around 200 °C and a second to high-temperature paraelectric cubic (*Pm-3m*) phase at around ~ 350 °C [12]. The high-resolution TEM results of Doret et al.

suggested that the transition from FE- *R3c* to AFE-orthorhombic (*Pnma*) phase in the range of 200 to 300 °C then the orthorhombic sheets immediately transform into tetragonal phase at 300 °C for NBT ceramics [13, 14]. The cobalt substitution on the B-site of NBT undergoes a phase transition from FE-*R3c* to modified *Pnma* phase within low temperature (200 °C) but not up to T_{max} , and the intermediate AFE phase was suppressed. Such a case was attributed to the compositional fluctuations [15]. On the other hand, neutron diffraction investigations indicated that the intermediate AFE-tetragonal phase has an anti-parallel displacement of A and B-site cations [16]. According to Wang et al. (0.95 – *x*)NBT-*x*KBT-0.05BT ceramics exhibited a phase transition from FE-*R3c* to AFE-*P4bm* at depolarization temperature (T_d) [17]. Vakhrushev et al. reported that the presence of ferroelectric rhombohedral clusters within a non-polar tetragonal matrix was associated with the relaxor character of NBT [18]. The aforementioned reports clearly indicate the temperature-dependent phase transition in NBT and NBT-based relaxors is complex and still contradictory.

Grain size plays a significant role in temperature-dependent dielectric performances of NBT-based ceramics [19, 20]. According to Khauta et al. the temperature-dependent XRD revealed the suppression of the *R3c* phase with reduced tetragonality at 200 °C for 0.2 μm NBT, though temperature-dependent dielectric analysis is still required. [19]. Zhao et al. have reported that the dielectric anomaly at 200 °C of pure NBT ceramics vanishes and a small bend appears instead of a dielectric peak at T_c , which reveals the critical dielectric behavior of 100 nm grains. But, the actual mechanism is remained unclear [20]. Therefore, the sub-micron to large grain-sized phase pure NBT ceramics under various sinter conditions and their systematic research is still required.

Hence, in this work, we have presented the influence of grain size on FE to AFE phase transition via temperature-dependent dielectric measurements on NBT system with different grain sizes such as sub-micron, micron and large-micron. Also, report the optimum grain size required for the best ferroelectric and dielectric properties based on the structural as well as ferroelectric analysis of pure NBT. Finally, different grain sizes were analyzed as a function of temperature to evaluate the ferroelectric phase

transition as a function of the electro-caloric effect and energy storage density.

2 Experimental

Solid-state synthesis route (SSR) was used to prepare the different grain size $\text{Na}_{0.5}\text{Bi}_{0.5}\text{TiO}_3$ ceramics. Initially, the stoichiometric amount of dried Sigma Aldrich oxides; Na_2CO_3 (99.5%), Bi_2O_3 (99.9%), and TiO_2 (99.8%) were mixed well by mortar and pestle for half an hour (30 min). The mixed powders were calcined at 850 °C for 3 h. Then, binder PVA (polyvinyl alcohol) was added with the calcined powders and mixed in a mortar by hand granulation. Afterward, this mixture was compacted to pellets of 13 mm diameter and 1 mm thickness under 9 MPa pressure by hydraulic press. The pellets were sintered at 1180 °C for 10, 20 and 240 min where the PVA was removed at around 300 °C. Then, the diameter of sintered pellets was measured using screw gauge as 11.74 mm, 11.27 mm and 11.05 mm for 10 min, 20 min and 240 min. The surface of the sintered pellets was polished down to a thickness of ~ 0.6 mm for further characterization. The density of the pellets was found by Archimede's method and the density of the pellets is above 97% of the theoretical density. The structure of NBT ceramics was characterized using powder X-ray diffraction (PANalytical X'pert PRO). The detailed crystal structure refinement was carried out using the Rietveld analysis program Jana2006 package [26]. Each pellet was under X-ray diffraction for over 30 min. Hence, the X-rays should be deeply penetrated through the samples and gives better results for refinement. Field emission scanning electron microscope (FE-SEM, Quanta 250FEC) was used to examine the fractured surfaces of the NBT ceramics. The Micro Raman spectrometer (Jobin Yvon) was used to record the room temperature Raman spectrum with argon-ion lasers of 532 nm wavelength. The silver paste was applied on both the sides of the polished pellets for temperature (RT to 450 °C) and frequency (1 kHz–100 kHz) dependent dielectric measurements using a Hioki 3532–50 LCR meter. With a Precision ferroelectric tester system (Radiant Technologies), we measured the polarization–electric field hysteresis loops (P–E loops).

3 Results and discussion

Figure 1a, b and c show the FE-SEM images of the fractured surface of pure NBT samples sintered at 1180 °C for 10 min, 20 min, 240 min and named them as sub-micron, micron and large-micron NBT ceramics, respectively. Based on the linear intercept method, the average grain size was determined and the average grain sizes are 0.38 μm , 1.23 μm , and 3.65 μm , respectively. For the 10 min sintered pellet, the grain growth was low. On increasing the sintering time to 20 min, explicit spherical and rectangular-shaped grains were seen. For further increase of sintering time to 240 min, distinct cuboidal-shaped grains with well-defined grain boundaries were detected. The average pore size and porosity (%) of NBT with different grain size ceramics are shown in Fig. 2a, b. It is noted that the two types of pores observed in sub-micron to larger micron such as (i) Residual pores (constant size = 0.3 to 1.2 μm range) and (ii) Macroscopic pores (represented by the pore size equal to grain size and larger) [21]. These pore sizes were calculated using the ImageJ software package. In sub-micron NBT a large number of small residual pores occurred than macroscopic pores due to the curtailed grain growth by low sintering time, leading to a high value of total pores and porosity (8.2%) as shown in 2(b). The residual and macroscopic pores were formed at 20 min sintering time and have low porosity (4.8%). Figure 2a illustrates that the average size and porosity (6.8%) of macroscopic pores increase as sintering time rises to 240 min due to the volatilization of Na and Bi ions. Hence, from the micrographs, it is clear that the grain size and porosity depend upon sintering time and as the sintering time increases grain size also increases [22, 23]. The important factor is the highly dense microstructures are required to improve dielectric and ferroelectric properties while average grain size directly affects the structural, dielectric permittivity and remnant polarization as discussed below.

The room temperature X-ray diffraction pattern is shown in Fig. 3a for three different samples of different grain sizes. Diffraction patterns were indexed to pseudo-cubic indices which is typical for ABO_3 perovskite structures. No secondary phases were observed related to the impurity phase and hence all the synthesized samples were phase pure. Enlarged view of the pseudo-cubic peaks $\{111\}_{\text{pc}}$ and $\{211\}_{\text{pc}}$ in log scale are shown in Fig. 3b, c for better

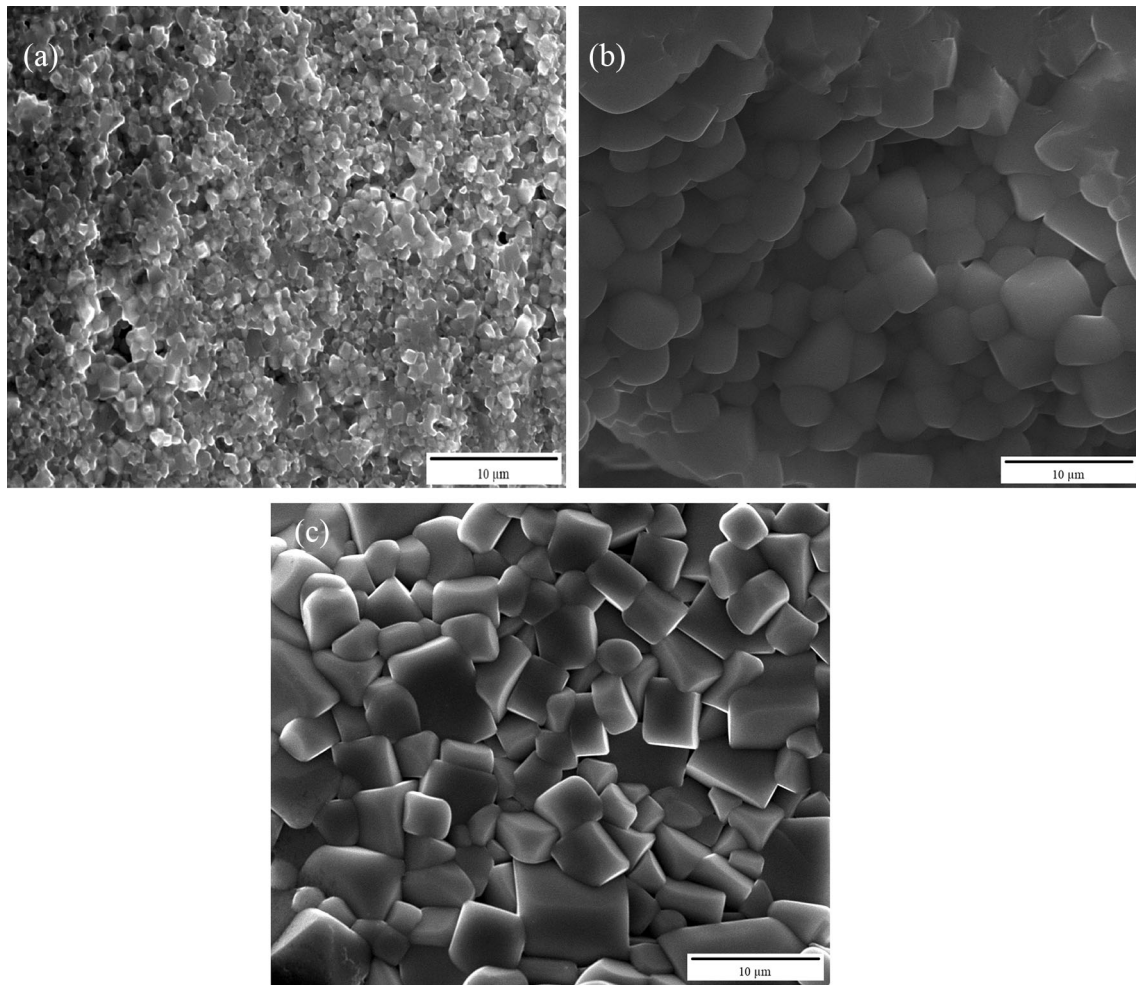


Fig. 1 FE-SEM micrographs of $\text{Na}_{0.5}\text{Bi}_{0.5}\text{TiO}_3$ ceramics sintered at **a** 10 min **b** 20 min and **c** 240 min

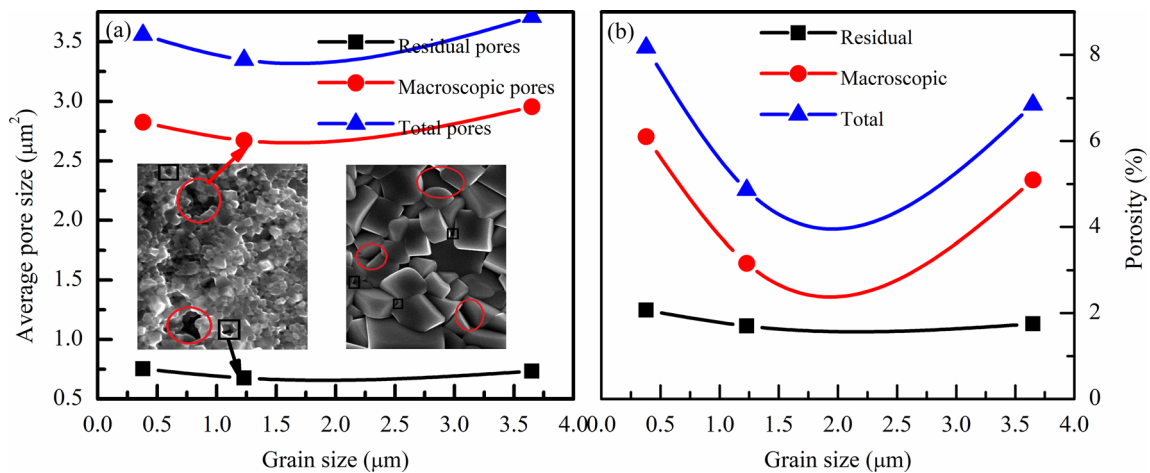


Fig. 2 **a** Average pore size **b** porosity (%) of sub-micron, micron and large-micron NBT ceramics

observation. Both the $\{111\}_{\text{pc}}$ and $\{211\}_{\text{pc}}$ split into two peaks (111) & (11-1) and (211) & (21-1) respectively that were identified in micron and large-

micron NBT along with the appearance of superstructure reflection of $\frac{1}{2}(311)$. But the sub-micron NBT showed very weak superlattice reflection $\frac{1}{2}(311)$

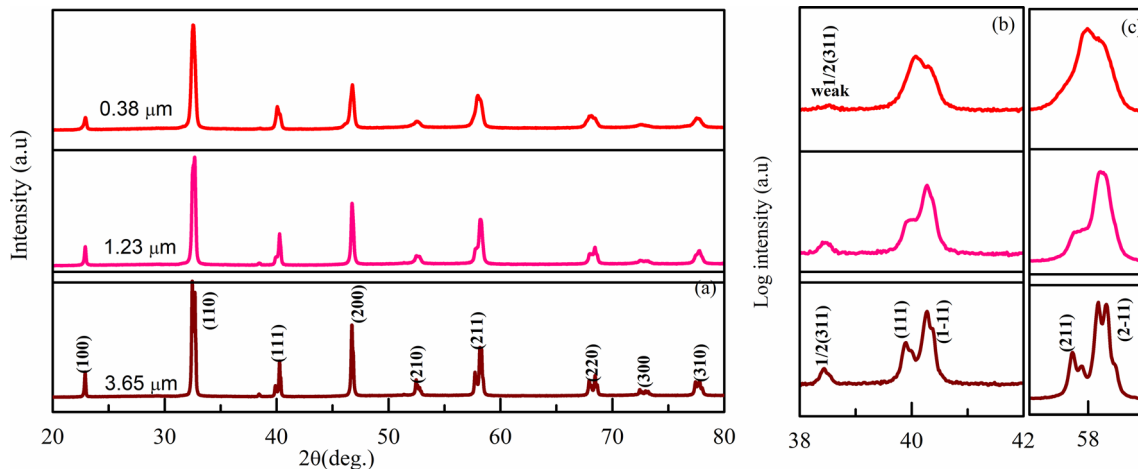


Fig. 3 a XRD patterns of sub-micron (0.38 μm), micron (1.23 μm) and large-micron (3.65 μm) samples (b and c) Evaluation of diffraction peaks enlarged view of $(111)_{\text{pc}}$, $(200)_{\text{pc}}$, and reflections

and peak broadening taking place instead of splitting of $\{111\}_{\text{pc}}$ and $\{211\}_{\text{pc}}$ peaks. The broadening of FWHM of X-ray diffraction peaks in sub-micron NBT can be related to the crystallite size and lattice strain effects [1]. For all the NBT samples, the induced lattice strain (ϵ) was found from the slope of the Williamson–Hall (W–H) plot and the crystallite size (D) was determined using both Scherrer’s formula,

$$D = \frac{n\lambda}{\beta \cos\theta} \quad (1)$$

and W–H method by the equation,

$$\beta = \frac{n\lambda}{D \cos\theta} + 4\sin\epsilon \quad (2)$$

where β -FWHM of XRD peak, n - dimensionless constant = 0.9, λ - wavelength of Cu $K\alpha$ radiation = 1.5406 \AA [24, 25] and the calculated values are listed in Table 1. According to Table 1, the crystallite size calculated from Scherrer’s formula is larger for all the NBT samples compared to that of using the W–H plot but the trend is the same. This is because the diffraction peak broadening (β) in the W–H plot is the combined effect of crystallite size (D) and lattice strain (ϵ), whereas in Scherrer’s equation the size effect alone contributes to peak broadening. Moreover, the induced lattice strain is decreased substantially as a function of increasing grain size, which reduces the broadening in FWHM of large-micron NBT. The observations of weak superlattice reflection and large peak broadening along with huge lattice strain and small crystallite size revealed that the sub-micron NBT exhibits a defect structure.

Structural refinement was carried out using the Rietveld analysis program Jana2006 package [26]. Rietveld refinement parameters for given space group, the lattice parameters, atomic position, atomic occupancies, 2θ zero shift, scale factor, 36 polynomial background parameters applying Legendre polynomials model, pseudo-Voigt and asymmetry parameter. The atomic occupancies of A site = $\text{Na}_{0.5}\text{Bi}_{0.5}$ and B site = Ti sites of the perovskite structure (ABO_3) were chosen according to the nominal composition. Initially, the XRD pattern was refined using a monoclinic Cc structure (figure not shown). The poor fit for representative pseudo-cubic peaks $\{110\}_{\text{pc}}$, $\{111\}_{\text{pc}}$ and $\{211\}_{\text{pc}}$ indicated that the synthesized ceramics were not crystallized in monoclinic (Cc) structural symmetry. Rather, the rhombohedral ($R3c$) crystal structure nicely accounted for all the Bragg profiles and which is similar to that of pure NBT as recently reported by Anupam Mishra et al. [27, 28]. Figure 4a–c show the Rietveld refined diffraction pattern of the sub-micron, micron and large-micron NBT samples, respectively. Insets of Fig. 4a–c reflect the superlattice peak near 38° which fitted very well along with the main rhombohedral reflections, after the fine cycle of refinement for all parameters with $R3c$ space groups. The unit cell parameters generated in refinement are tabulated in Table 2. It was observed that the unit cell volume increases as a function of increasing grain size. But, the crystal system remains unchanged and confirmed that the rhombohedral ($R3c$) structure was stabilized for all the grain size samples at room temperature. Also, the best fit was obtained for micron (1.23 μm) grain size ceramics. In comparison,

Table 1 Grain size, crystallite size and lattice strain of sub-micron, micron and large-micron NBT ceramics

Sample	Grain size (μm)	Crystallite size (nm)		Lattice strain (ε)
		W–H plot	Scherrer's equation	
Sub-micron	0.38	59.51	68.24	5.1083×10^{-5}
Micron	1.23	65.71	71.98	$- 3.2819 \times 10^{-5}$
Large-micron	3.65	89.45	92.34	$- 3.0542 \times 10^{-6}$

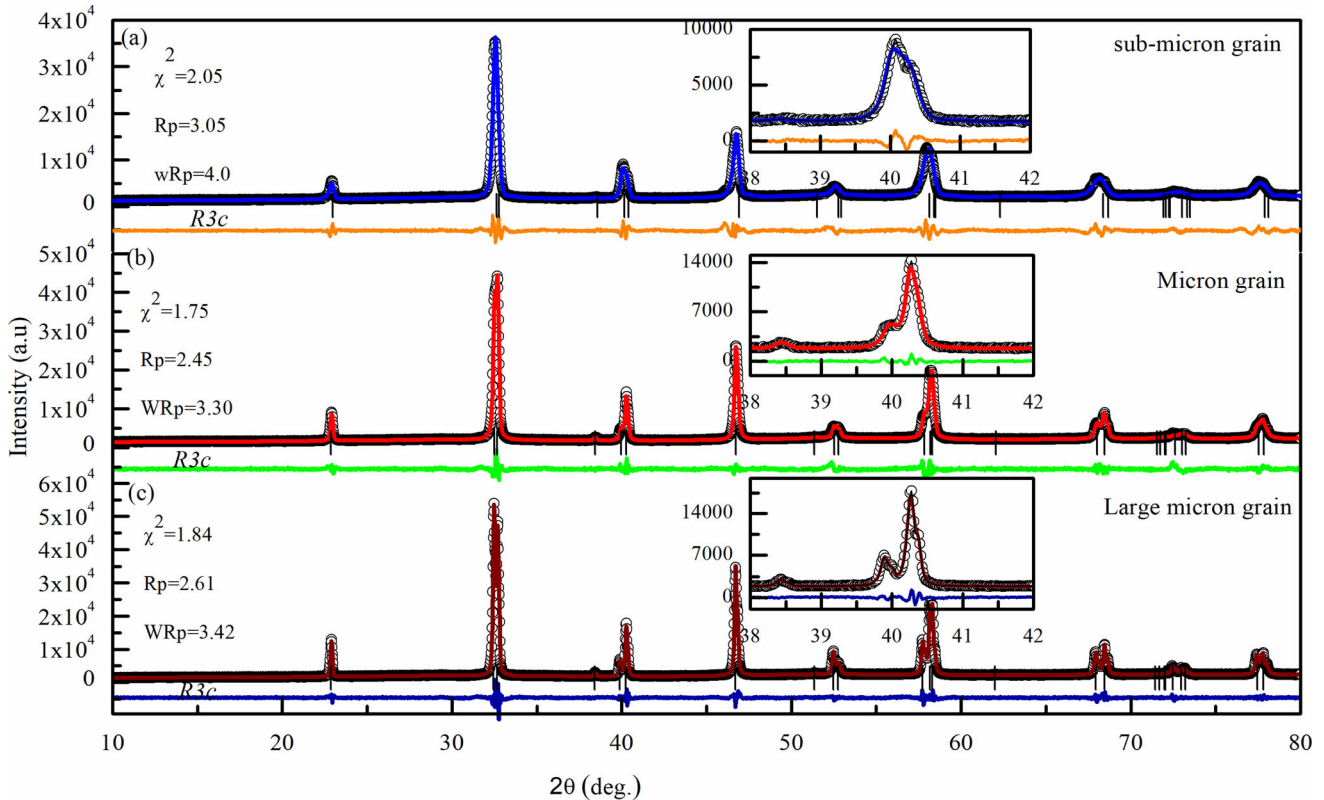


Fig. 4 a–c Rietveld refinement of XRD patterns of sub-micron, micron and large-micron samples insert shows selected region pc (pseudocubic) peaks of (111)_{pc} and (200)_{pc} reflections

the sub-micron NBT exhibits a weak superlattice reflection around 38° illustrated in Fig. 4c due to the small anti-phase TiO₆ octahedral tilting, thus reduction in the R3c unit cell volume [29].

The TiO₆ octahedral tilting angle was determined for each grain-size NBT using the formula:

$$\theta_{tilt} = \frac{180 - \theta}{2} \tag{3}$$

where θ < Ti–O–Ti bond angle measured from the refinement data and visualized using VESTA software [35, 36] and the results were sorted in Table 3. Fig. 5a, b clearly illustrates that the octahedral tilting angle deviated significantly from 6.54° to 9.51° with an increase in grain size (0.38 μm–3.65 μm). These deviations generate three short and three long metal–

oxygen (Ti–O) bonds in the TiO₆ octahedra of all the NBT samples [30] and the average bond length is shown in Table 3. Based on the structural analysis, the sub-micron NBT reveals a defective R3c structure confirmed by the weak superlattice reflection which is the result of small octahedral tilting and peak broadening effects.

The Raman spectra in the range of 50–1200 cm⁻¹ were recorded at room temperature and deconvoluted as shown in Fig. 6a. Usually, the Raman spectrum of pure NBT is divided into four major bands and labeled as A, B, C, and D, respectively. The first band (A region: 50–200 cm⁻¹) was related to the two cations distortion in the A-site (Na/Bi–O) of the NBT system. In the A region, the low frequency of around

Table 2 Rietveld refinement structural parameters of sub-micron, micron and large-micron NBT ceramics

Grain size	0.38 μm	1.23 μm	3.65 μm
Space group	<i>R3c</i>	<i>R3c</i>	<i>R3c</i>
a(Å)	5.4639	5.4781	5.4787
b(Å)	5.4639	5.4781	5.4787
c(Å)	13.4634	13.5301	13.5533
V(Å ³)	348.1	351.6	352.3
Density (ρ)	97.5%	97%	95%
d111/d-111-1	1.0070	1.0042	1.0030
Na/Bi <i>x</i>	0.0000	0.0000	0.0000
<i>y</i>	0.0000	0.0000	0.0000
<i>z</i>	0.2512	0.2626	0.2845
Ti <i>x</i>	0.0000	0.0000	0.0000
<i>y</i>	0.0000	0.0000	0.0000
<i>z</i>	0.0006	0.0054	0.0092
O <i>x</i>	0.0124	0.1277	0.1547
<i>y</i>	0.1254	0.3449	0.4994
<i>z</i>	0.01375	0.0723	0.1292
R _p	3.05	2.45	2.61
χ^2	2.05	1.75	1.84
WR _p	4.00	3.30	3.42

50–80 cm^{-1} is associated with Bi–O vibrations and 100–200 cm^{-1} is related to Na–O vibrations. Due to the heavier mass of Bi (208.98 u) than Na (22.98 u), the Bi–O vibrations were obtained in the low-frequency region [31]. The second band (B region: 200–350 cm^{-1}) is associated with the B site Ti–O vibrations. The third band (C region: 400–650 cm^{-1}) is dominated by TiO₆ octahedral tilting vibrations and the last band (D region: 743–842 cm^{-1}) can be related to the oxygen displacements [31, 32]. A two-unit irreducible representation from group theory has a 30 optical phonon mode as $5A_1 + 5B_1 + 10E$, where both $4A_1 + 9E$ modes are Raman and Infrared active, $5B$ modes are quiet, and one $A_1 + E$ mode is acoustic. The optical modes are split into longitudinal and

transverse modes. Figure 6a shows all the Raman modes relevant to Na–O, Bi–O, Ti–O, TiO₆ and oxygen vibrations were noticed as well as rhombohedral structure in agreement with previous reports [31, 33]. Therefore all the synthesized ceramics retained rhombohedral *R3c* structure for different grain sizes which is consistent with XRD results. Zhang et al. reported that increasing doping content in NBT could be divided the C band into C' and C'' modes [34]. Surprisingly note that the increasing grain size also offers the same effect in NBT ceramics as illustrated in the fitting curve 6 (a) and magnified view of Fig. 6c. This splitting of Raman modes indicates the increase of structural distortion with increasing grain size. This is due to increasing TiO₆ octahedral distortion (Δ_{oct}) from sub-micron to large-micron NBT, which can be estimated using the Ti–O bond length relation:

$$\Delta_{oct} = 1/6 \sum_1^6 \left[\frac{\delta n - \langle \delta av \rangle}{\langle \delta av \rangle} \right]^2 \quad (4)$$

where δn and δav are the individual and average interatomic Ti–O bond lengths [35]. According to the findings (Table 3), the large-micron NBT exhibits a very large octahedral distortion (81.35×10^{-4}) compared to that of sub-micron NBT (2.1×10^{-4}). Among all the samples the large-micron NBT exhibits a low-intensity peak in all the Raman modes as shown in Fig. 6a. This can be proposed that the increasing anti-phase octahedral tilting ($a^-a^-a^-$) improves the rhombohedral in large-micron NBT. The sub-micron NBT shows an increase in FWHM of Na–O, Ti–O and TiO₆ vibration bands due to the phonon scattering by defects and large lattice strain effects [37]. The enlarged Na–O vibration shown in Fig. 6b indicated that the frequency softening takes place in sub-micron NBT which is $\sim 10 \text{ cm}^{-1}$ lower than the micron and large-micron NBT ceramics. This was arising due to the weakening of the A–O phonon mode. The

Table 3 Bond length, bond angle, octahedral tilt and distorted TiO₆ octahedra of different grain size NBT ceramics

Sample	Average Bond length (Å) Ti–O	Bond angle (deg.)		Tilt angle (deg.)	TiO ₆ octahedral distortion ($\times 10^{-4}$)
		Ti–O–Ti	O–Ti–O		
Sub-micron	1.9585	166.91	177.95	6.54	2.10
Micron	1.9553	165.76	175.48	7.12	66.93
Large-micron	1.9729	160.98	163.91	9.51	81.35

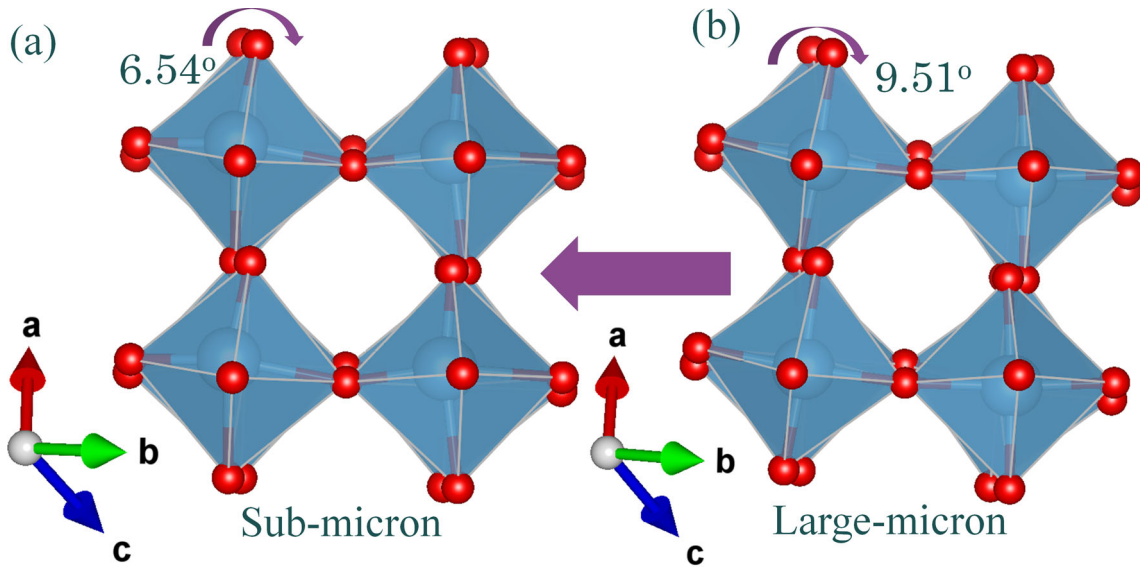


Fig. 5 a, b Magnified view of two adjacent interconnected TiO_6 octahedral tilt angle of sub-micron and large-micron NBT samples

magnified view of TiO_6 Raman mode is displayed in Fig. 6c clearly indicated the FWHM decreased with increasing grain size. It is evident for pronounced rhombohedral distortion takes place at high sintering time. The FWHM can be related to the phonon relaxation time using the relation [37]:

$$\tau = \frac{1}{c\pi\Gamma} \tag{5}$$

where τ -phonon relaxation time, c -velocity of light and Γ - FWHM of phonon mode. The relaxation time (τ) was calculated for Ti–O and Na–O modes and fitted for different grain size NBT samples as shown in Fig. 6d, e, respectively. Both results illustrated that the sub-micron NBT has less relaxation time due to the broad and weak phonon modes with a large lattice strain effect. This can be correlated with the weak superlattice reflection as discussed in x-ray diffraction results.

Temperature-dependent dielectric permittivity (ϵ_r) and dielectric loss ($\tan\delta$) of pure NBT ceramics with various grain sizes were measured at 1 kHz to 100 kHz and are shown in Fig. 7a–c. The dielectric permittivity (ϵ_r), as well as loss ($\tan\delta$), decreases with an increase in frequency and loss maximum shift towards higher temperatures as the frequency increases which was consistent with relaxor ferroelectrics [12, 16, 19]. The obtained dielectric parameters are tabulated in Table 4. Among the different grain-size ceramics, 1.23 μm sample showed maximum dielectric permittivity and the highest Curie

temperature ($T_c \sim 340^\circ\text{C}$). The different sintering times in preparation of sub-micron to large-micron samples can induce a difference in microstructure, lattice distortion, and density which cause the changes in ϵ_r and ϵ_m [38]. Cai et al. have recently reported [39] that the ceramics with a composition of $(\text{Bi}_{0.5}\text{Na}_{0.5})_{0.94}\text{Ba}_{0.06}\text{TiO}_3$ sintered at different times exhibit higher ϵ_m value at micron grain size. As reported in earlier studies, the maximum permittivity (ϵ_m) is decreased when grain size exceeds 2 μm [3]. The observed decrease in the porosity of micron NBT (Fig. 2b) could also be considered as an extrinsic factor contributing to increase in the dielectric permittivity. [40]. Figure 7b, c clearly illustrate that micron and large-micron samples exhibited two broad dielectric anomalies, one in the temperature range below 250 $^\circ\text{C}$ which refers to ferroelectric (FE)-rhombohedral ($R3c$) to antiferroelectric (AFE)-tetragonal ($P4bm$) transition. Another below 350 $^\circ\text{C}$ denotes the Curie temperature (T_c), and at T_c the structural phase transition occurred from AFE ($P4bm$) to paraelectric (PE)-cubic ($Pm-3m$) which is similar to the characteristic nature of NBT relaxor ferroelectrics [9, 12]. The dielectric dispersion is located below 200 $^\circ\text{C}$ in all the NBT samples and it does not involve any structural phase transition from $R3c$ to $P4bm$ [31]. Note that the dielectric dispersion temperature decreased with increasing grain size. However, in sub-micron NBT, there is only one well-defined phase transition which revealed the retaining of the ferroelectric phase up to Curie temperatures, as

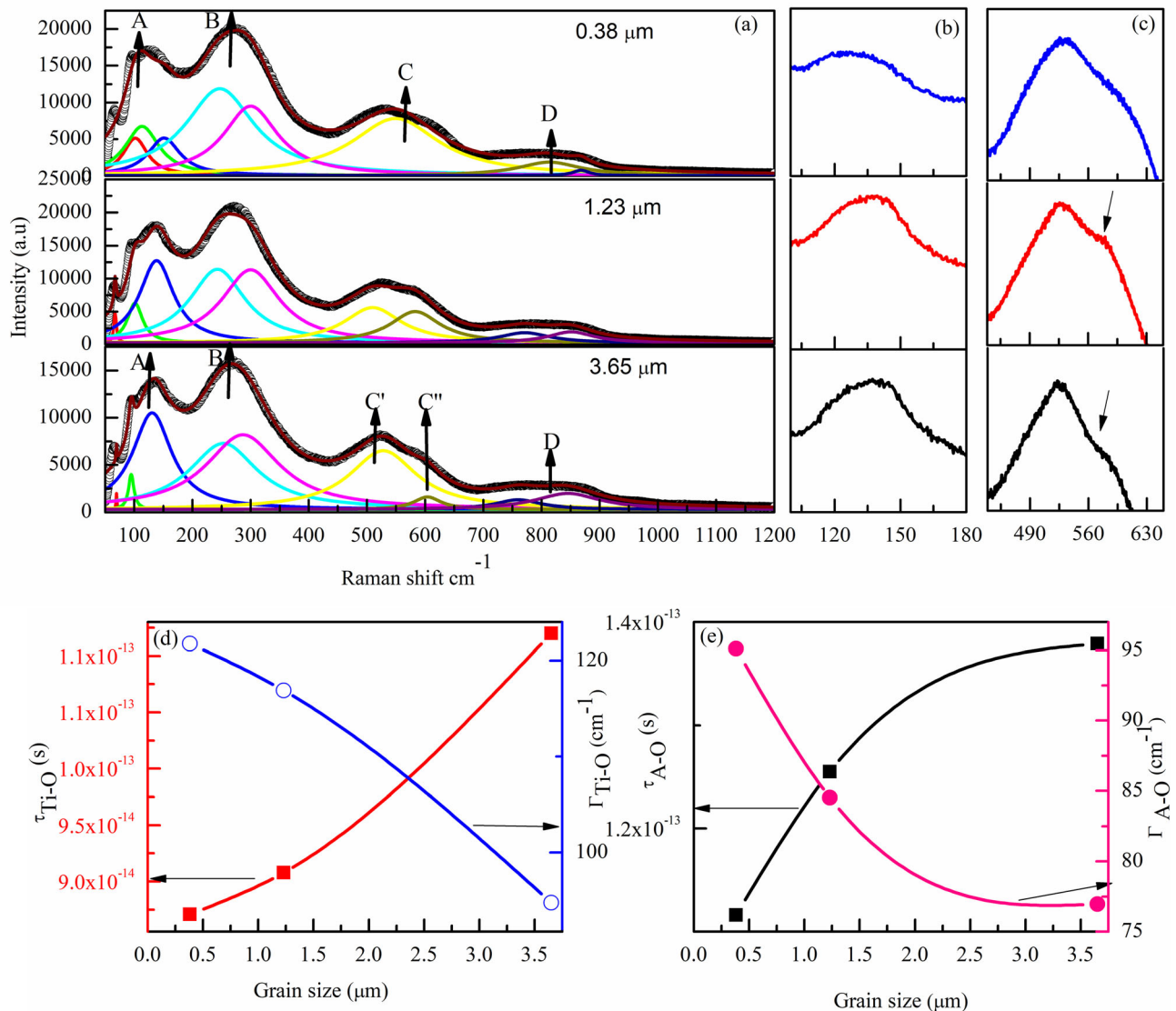


Fig. 6 **a** Deconvoluted Raman spectra for sub-micron to large-micron grain size (0.38, 1.23, and 3.65 μm) samples in the range 50–1200 cm⁻¹ **b** Enlarged view of Na–O and **c** TiO₆ octahedral

modes respectively for each grain size NBT samples, FWHM (Γ) and phonon relaxation time (τ) of **d** Ti–O and **e** A–O phonon modes as a function of grain size

shown in Fig. 7a. Generally, the NBT domain structure contains fine polar nanoregions (PNR) within the *R3c* structure at room temperature [31]. Figure 8a, b present the schematic diagram of FE and AFE orders at different thermal regions of sub-micron NBT as compared with micron NBT ceramics. The thermal energy affects the size and dynamics of PNRs. The size of PNRs increases as the temperature reaches freezing temperature (T_f), which prevents their dynamics as shown in Fig. 8. This static-PNR region of NBT is known as the non-ergodic region [41, 42]. As the temperature rises over T_f , the non-ergodic system transforms into an ergodic-relaxor, with

extremely dynamic PNRs [41, 43]. The freezing temperature decreases as grain sizes increase from sub-micron to large-micron as shown in Table 4, and non-ergodicity is inhibited in large-micron NBT near 100 °C Fig. 7c. This clearly shows that enhancing the sintering time disturbs the non-ergodic character of NBT and induces ergodic-relaxor behavior at low temperatures. Similarly, the low-temperature relaxor-like behavior was achieved by increasing BT content on NBT was reported by Guo et al. [44]. The low-temperature dielectric anomaly originates from the thermal evolution of PNR from *R3c* to *P4bm*, where the anti-phase $a^-a^-a^-$ (Glazer notation [45])

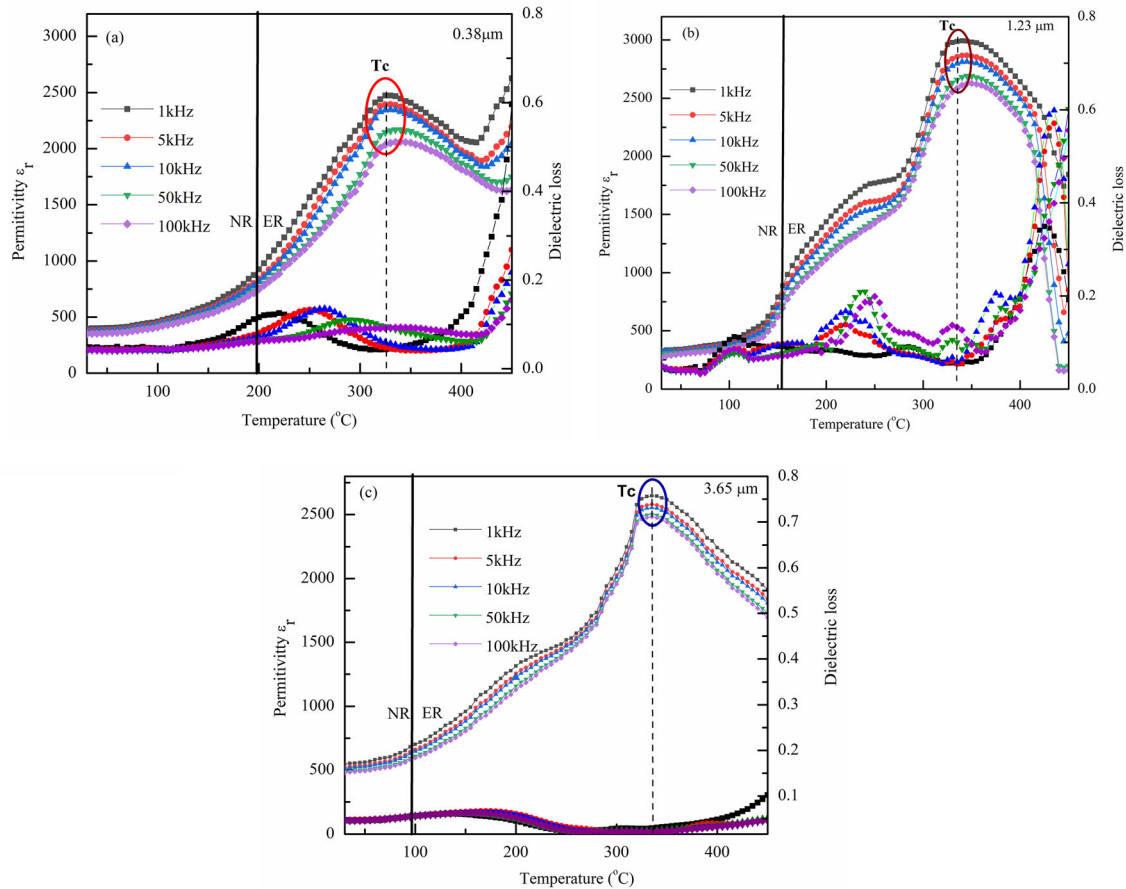


Fig. 7 Temperature dependence of the dielectric permittivity and dielectric loss tangent at 1 kHz–100 kHz of NBT ceramics different grain size **a** sub-micron **b** micron and **c** large-micron NBT

Table 4 Dielectric parameters (ϵ_r , ϵ_m , T_c , T_f and γ) of sub-micron, micron and large-micron NBT ceramics

Parameter	Sub-micron	Micron	Large-micron
Dielectric constant (ϵ_r)	339	283	572
Dielectric constant (ϵ_m)	2476	3016	2780
Freezing Temperature (T_f) °C	198	152	95
Curie Temperature (T_c) °C	325	340	335
Diffusivity (γ)	1.59	1.54	1.42

octahedral rotations changed into in-phase $a^0a^0c^+$ (Glazer notation [45]). In which the ferroelectric long-range order is diminished and the material subsequently transforms to AFE short-range order, as seen in micron and large-micron NBT Fig. 7b, c. The phenomenological residual stress model proposed that during PE to FE phase transition the cell volume of the ferroelectric material is increased at the Curie temperature (T_c) which results in maximum dielectric dispersion occurring around T_c [2, 3, 46]. Hence, the maximum dielectric dispersion was observed around T_c in the three different grain sizes shown in the

encircled region of Fig. 7a–c. After this phase transition, the internal stress of the material is increased due to each interconnected grain being constrained by its neighbors. Generally, this internal stress was relieved by the formation of tetragonal-90° domains [46].

Conversely, no dielectric shoulder was observed around 250 °C in sub-micron NBT corresponding to the FE- $R3c$ to AFE- $P4bm$ phase transition indicating the suppression of the intermediate AFE- tetragonal phase. The abnormal behavior of sub-micron NBT arises from the following aspects. Mainly the grain

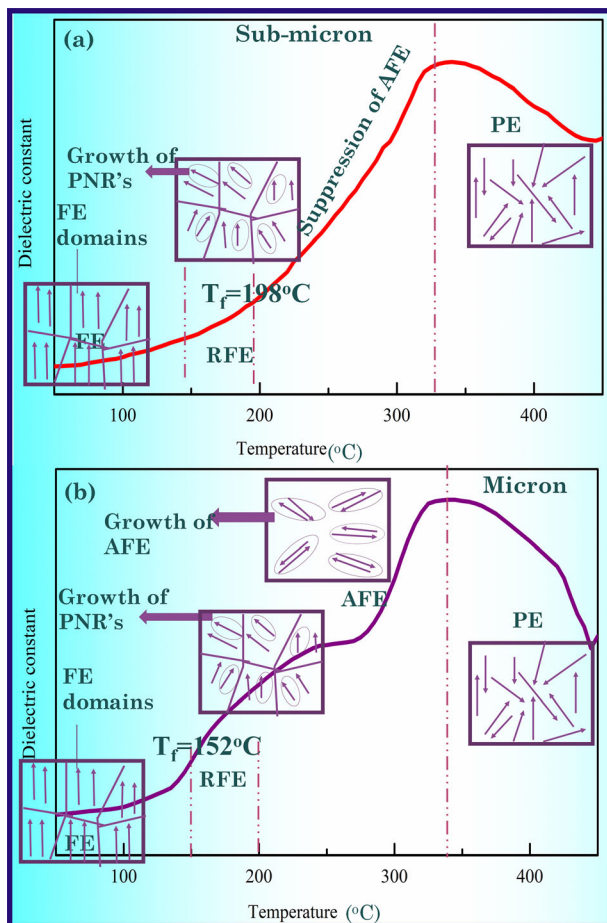


Fig. 8 Schematic diagram of FE and AFE order at different temperature regions of **a** sub-micron and **b** micron NBT ceramics

size effect plays an important role in the reduction of the AFE phase [20]. The domain size (d) correlated with grain size (g) by a simple relationship:

$$d \propto g^{1/2} \quad (6)$$

and this equation indicates even a small variation in grain size largely affects the domain size [3]. Tuttle et al. observed that the grain size ranging from 0.2 to 1 μm contains single 90° domain walls, and multiple domain walls were observed only for grain size $> 1 \mu\text{m}$ [47]. Also, the possibility to form domain twinning within fine grain ceramics is very low resulting in increasing internal stress throughout the grains as reported earlier [48]. Further, Zhao et al. proposed that the grain size reduced below critical size ($\sim 500 \text{ nm}$), the 90° domain does not form, and where the internal stress was not to be relieved. This unrelieved internal stress suppressed the tetragonal phase and triggers the phase close to cubic in BT ceramics [2]. Reducing grain size below 500 nm

(0.5 μm) and decreasing the lattice parameter along with the suppression of the tetragonal phase in sub-micron NBT should have a similar impact as in BT. Owing to this effect, the FE ($R3c$) to AFE ($P4bm$) phase transition is suppressed in sub-micron NBT, resulting in the absence of low-temperature dielectric anomaly. The previously reported effective medium approximation (EMA) model proposed that the stressed mono-domain dilutes the bulk permittivity for fine grain ceramics [49]. So the sub-micron NBT possesses low dielectric permittivity with the absence AFE phase. While increasing grain size $> 1 \mu\text{m}$, the permittivity also increases as the function of lowering dilution effect, but still only up to a limit at which any additional increase in grain size would result in stress relaxation through domain formation, resulting in a gradual reduction in dielectric permittivity (ϵ_r) [40, 50]. Therefore, the intermediate grain size achieved the maximum dielectric permittivity than large-micron NBT. Further, Fig. 9a–c show the $d\epsilon/dT$ vs. $T(^\circ\text{C})$ plot clearly illustrates the suppression in dielectric anomaly for sub-micron NBT sample as compared with micron and large-micron NBT around the FE-AFE transition (rectangular box shown in Fig. 9a). It additionally supports the possibility of suppressing the intermediate AFE phase for sub-micron NBT. Moreover, the suppression of the AFE phase was evident by structural and ferroelectric characterizations. From X-ray diffraction analysis, the weak superlattice peak and increased FWHM indicate the reduced size of domains [3]. The very small octahedral distortions with low sintering time result in weak dipole moments and are attributed to the low dielectric permittivity in sub-micron NBT. The small octahedral distortion and weak superlattice reflection with a low octahedral tilt angle in sub-micron NBT imply that it has less asymmetry distortions than larger grain NBT. This behavior of sub-micron NBT is related to the presence of the $R3c$ -nearly cubic phase transition in the dielectric anomaly. Besides, the Raman analysis for NBT exhibits variations in the A-O mode that could be sensitive to the antiferroelectric (AFE) phase [31, 40]. In sub-micron NBT, the decrease in octahedral tilting and slight softening of Na–O vibration around 128 cm^{-1} (which is $\sim 10 \text{ cm}^{-1}$ less than the micron and large-micron NBT) and less relaxation time of A-O phonon with large FWHM was strongly affecting the FE to AFE phase transition. However, the exact mechanism of intermediate AFE phase suppression in sub-

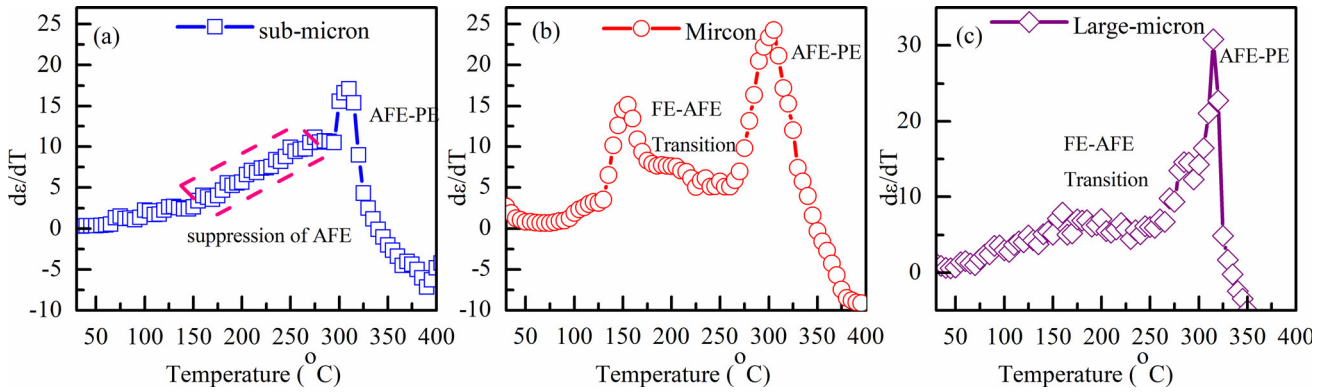


Fig. 9 $d\epsilon/dT$ vs. $T(^{\circ}C)$ plot at 100 kHz for **a** sub-micron, **b** micron and **c** large-micron NBT ceramics

micron NBT can be more precisely revealed by high-resolution TEM investigations.

The dielectric behavior of a relaxor ferroelectric can be explained using the Curie–Weiss law [51] which can be written as

$$\frac{1}{\epsilon_r} - \frac{1}{\epsilon_{max}} = \frac{(T - T_m)^\gamma}{C} \tag{7}$$

where T is the absolute temperature, C is the material constant. The diffusiveness γ of a normal ferroelectrics is 1 whereas the diffusiveness γ of an ideal relaxor ferroelectric is 2. Figure 10 shows the curve of $\log(1/\epsilon_r - 1/\epsilon_m)$ vs $\log(T - T_m)$ for the pure NBT ceramics with various grain sizes. The diffusive factor γ was 1.59, 1.54 and 1.42 for sub-micron, micron and large-micron NBT ceramics, respectively. The result indicated that the diffusiveness was high for the submicron grain-size sample and gradually decreases as increasing grain size. As a result of large stress in sub-micron NBT, the ferroelectric long-range order is weakening and domain wall motion is prevented. This can increase the value of diffusiveness.

Figure 11 shows the polarization–electric field (P – E) hysteresis loop of various grain-size ceramics at room temperature. Observation of the well-saturated P – E hysteresis loop confirmed the ferroelectric nature of the synthesized ceramics. Well-defined squared loops are seen for micron and large-micron NBT samples, while for sub-micron grain samples the loop slightly deviates from the square loop. Figure 11 (insert) presents the squareness (R_{sq}) of P – E hysteresis loop which can be determined using the empirical relationship of:

$$R_{sq} = \frac{P_r}{P_s} + \frac{P_{1.1Ec}}{P_r} \tag{8}$$

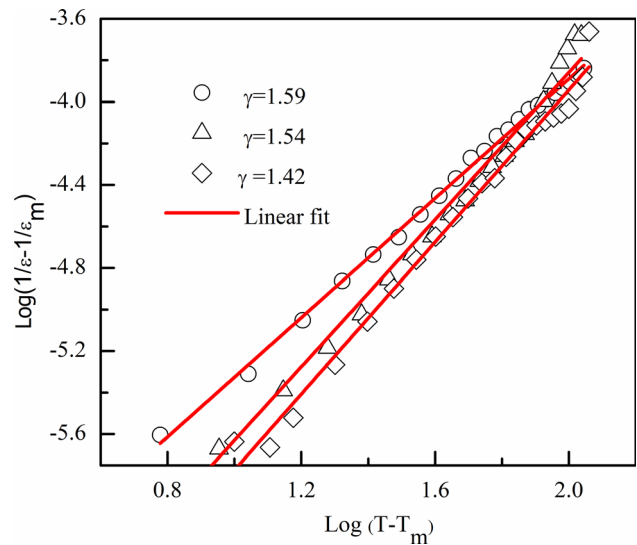


Fig. 10 Plots of $\log(1/\epsilon_r - 1/\epsilon_m)$ vs $\log(T - T_m)$ at 100 kHz for the sub-micron to large-micron NBT ceramics

where P_r , P_s and $P_{1.1Ec}$ are remanent polarization, saturation polarization and polarization at an electric field equal to 1.1 coercive field respectively [52]. $R_{sq} = 2$ for an ideal ferroelectric square loop [52, 53]. In our case, the micron ($R_{sq} = 1.94$) and large-micron ($R_{sq} = 1.97$) samples possess the perfect square loop ($R_{sq} \sim 2$) comparatively the sub-micron samples (1.85). Thus the shape of the loop indicates the improvement of ferroelectric performance with increasing sintering time. Remnant polarization of sub-micron, micron and large-micron NBT were 19.36, 43.12 and 27.57 $\mu C/cm^2$ respectively. The remnant polarization and coercive fields were strongly influenced by sintering time from these results. However, the maximum value of remnant polarization $P_r \sim 43.12 \mu C/cm^2$ with coercive field

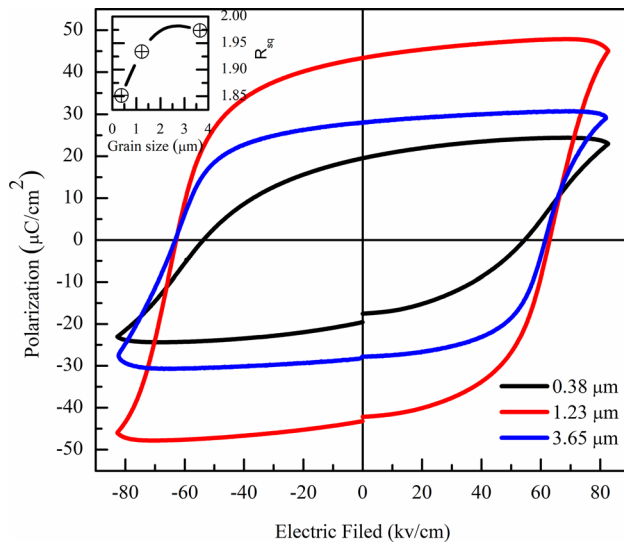


Fig. 11 Room temperature P–E hysteresis loops of sub-micron, micron and large-micron NBT samples (inset fig. squareness of the loop)

$E_c \sim 63$ kV/cm was obtained for 1.23 μm grain size ceramics. The low value of polarization in the sub-micron grain size was due to grain boundary effects which lower the dielectric constant. According to Khatua et al. when the grain size attained the sub-micron range the piezoelectric response and the domain switching is reduced in bulk-NBT ceramics [19]. The decrease in grain size reduces electric polarization due to increased grain boundary as reported by Alguero et al. [54] also this happened to the motion of domain wall hindering due to defects [7]. Room temperature XRD and Raman analysis have confirmed that defects arise in sub-micron NBT, which might be the reason for reducing P_r . An enhanced ferroelectric property for 1.23 μm grain size with high remnant polarization indicated improved non-180° domain reorientation and rapid domain switching. Polarization reversal within a ferroelectric domain was easier and increases the mobility of domain walls in micron grain than in sub-micron. Large micron grain size sample showed low ferroelectric properties due to the relatively low density [8], which adversely affects P_r (remnant polarization) and E_c (coercive field). Dragan clearly denoted that the effect of grain boundaries and porosity strongly affect domain wall switching in PZT ceramics [55]. Thus increasing the size and number of macropores in large-micron NBT could have reduced the ferroelectric performances. Moreover, it can be concluded that optimum grain size with reducing porosity

elevates the remnant polarization and coercive field, where increased mobility, domain reorientation, and polarization switching supports to enhanced piezoelectric [21, 56], dielectric and ferroelectric properties of micron-NBT ceramics.

For each NBT sample, the temperature-dependent P–E loop was carried out for three specific regions namely ferroelectric (FE), relaxor ferroelectric (RFE) and anti-ferroelectric (AFE) to confirm the abnormal behavior of sub-micron NBT as shown in Fig. 12a–c. In Fig. 12b, c the square-type PE loop became slim at 120 °C, indicating the transition from FE to RFE, and its shape changed to pinching of hysteresis at 180 °C, indicating the RFE to AFE phase transition. The change in the shape of the loop reduces the ferroelectric properties due to the formation of microdomains from macro domains in the relaxor state and the evolution of microdomains into PNRs in the AFE region [57, 58]. Although the relaxor loop is stable up to the maximum temperature range in sub-micron NBT Fig. 12a, it does not exhibit a pinching of hysteresis loop, reconfirming the unusual nature of the sample. The absence of pinching hysteresis demonstrated suppression of the AFE phase and evidence for dielectric results.

Figure 12a–c declare that the coercive field decreases sharply as a function of increasing temperature with a little variation in P_r and P_{max} values for all NBT samples. From the temperature-dependent PE loops the recoverable energy storage density (W_{rec}) during the process of charging and total energy storage density (W_{total}) were investigated using the following relation [59]:

$$W_{rec} = \int_P^{P_{max}} E dP \quad (9)$$

$$W_{total} = \int_0^{P_{max}} E dP \quad (10)$$

where P and P_{max} represent the remanent and saturation polarization respectively and E represents the applied electric field as 55 kV/cm. Figure 13 (a) differentiates the recoverable energy storage density W_{rec} (yellow color area) for FE vs AFE regions as the function of the electric field 55 kV/cm. The energy storage efficiency (η) is measured using the relation [59]:

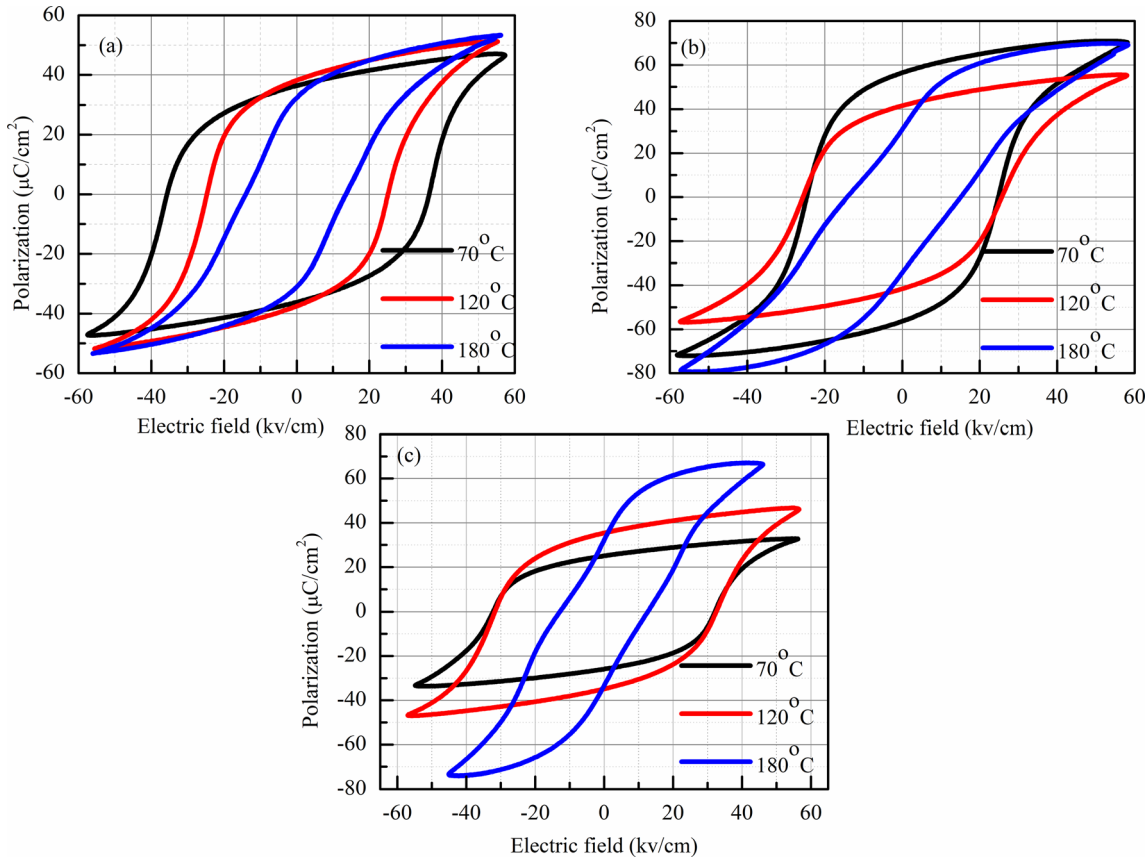


Fig. 12 (a) Temperature dependence of P–E loop measured for ferroelectric, relaxor, and antiferroelectric (70 °C, 120 °C, and 180 °C) of a sub-micron b micron c large-micron NBT

$$\eta = \frac{W_{rec}}{W_{total}} \times 100\% \tag{11}$$

The estimated W_{rec} and η values of each specified region for sub-micron, micron and large-micron samples are shown in Fig. 13b, c. The PE loop of large-micron NBT gives high efficiency near room temperature compared to other samples in the FE region. This is due to the increasing sintering time hindering the macroscopic domains at low temperatures and encouraging the RFE near 70 °C. The result coincides with the temperature-dependent dielectric data. The size of macro domain > micro domain > PNRs, therefore the PNRs are easily aligned with the use of an external field. Hence the AFE region of micron and large-micron grains has achieved the maximum recoverable energy storage density than other regions. A large W_{rec} and efficiency of 0.55 J/cm³ and 26.12%, respectively, were achieved in the AFE region by micron NBT in the temperature range of 180 °C, which is considered to be the best performing material for energy storage applications. The

result was comparable with previous literature [60, 61].

To evaluate the electro-caloric effect (ECE) for NBT samples, the temperature-dependent P–E loops were taken for different applied electric fields of 35, 45 and 55 kV/cm. The ECE parameters of the reversible adiabatic change in temperature (ΔT) and isothermal change in entropy (ΔS) can be estimated using Maxwell’s relation as follows [59]:

$$\Delta S = -\frac{1}{\rho} \int_{E1}^{E2} \left(\frac{\partial P}{\partial T} \right) dE \tag{12}$$

$$\Delta T = -\frac{1}{\rho C_p} \int_{E1}^{E2} T \left(\frac{\partial P}{\partial T} \right) dE \tag{13}$$

where ρ is the density of the pellets as noted in Table 1, C_p refers the specific capacity of the NBT sample as taken from the literature [62], $E1$ and $E2$ implies the starting and final applied electric fields respectively, $\left(\frac{\partial P}{\partial T} \right)$ defines the change in the upper part

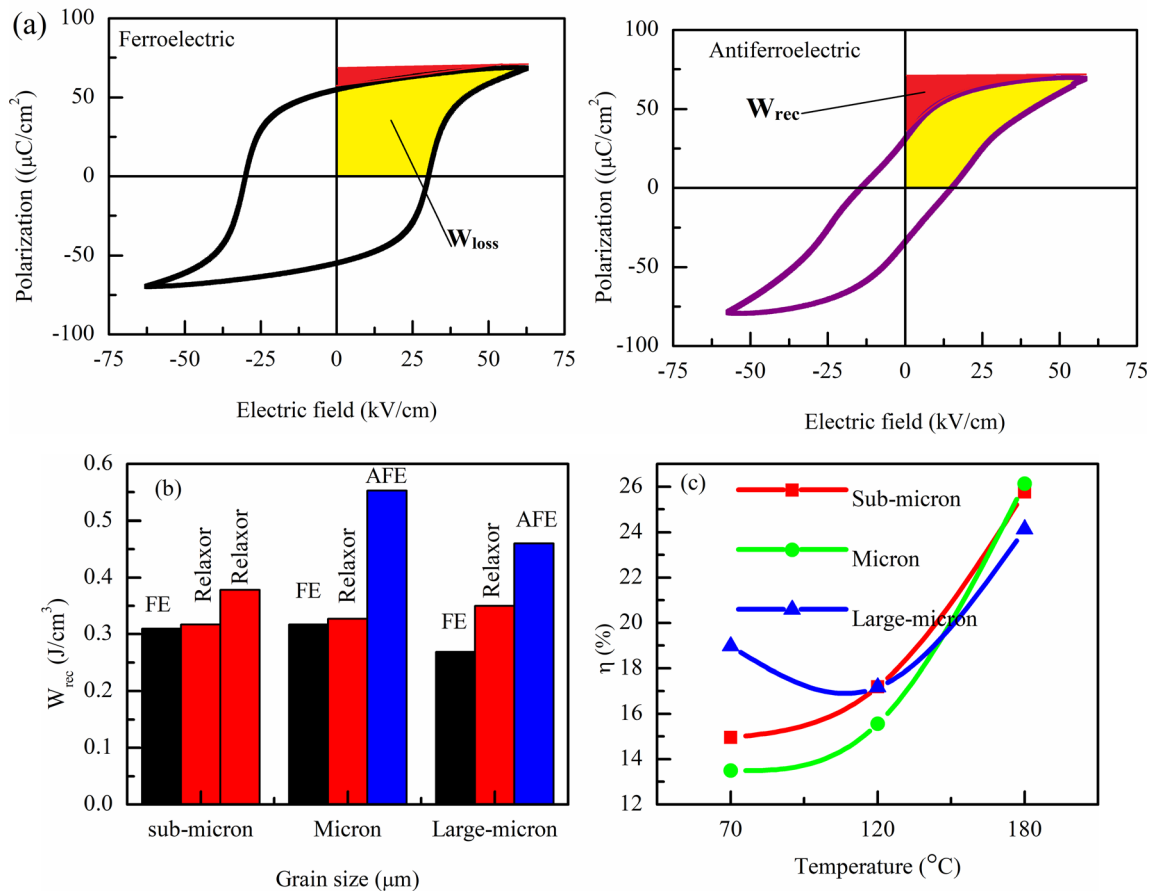


Fig. 13 **a** Schematic diagram of P–E loop for energy storage calculation. **b** Grain size vs recoverable energy storage density (W_{rec}) for FE, RFE and AFE regions. **c** Temperature-dependent energy storage efficiency for sub-micron, micron and large-micron NBT

of polarization in the P–E hysteresis loop to temperature. Figure 14a–c depict the change in polarization as a function of temperature and electric fields. With increasing the applied field strength, initially, the polarization also increases with temperature. The highest polarization variation was recorded for all samples at around 100 °C for the low field (35 kV/cm) due to the FE to the relaxor phase transition. After this transition point, polarization gradually rises to 170 °C for micron and large-micron samples then the polarization drops up to 180 °C for both the samples. This clearly depicts the onset of the FE to AFE phase transition. However, in sub-micron NBT, the polarization constantly rises for the fields of 35 and 45 kV/cm, while it gradually lowers very little from 100 °C for the field of 55 kV/cm. This demonstrates that the submicron sample contains solely a FE to the relaxor phase transition.

The ECE parameters were estimated using the procedures described in previous work [59][59] and

are shown in Fig. 15a–b. The significant variation in polarization leads to a greater change in entropy (S) of the materials as shown in Fig. 15a, which tends to enhance the adiabatic temperature change. All of the NBT samples have negative ECE as illustrated in Fig. 15b, which is consistent with previous results [64, 65]. The maximum ΔT of -0.81 K was observed in micron-NBT samples at ~ 60 °C for 55 kV/cm. The substantial ECE was achieved at lower temperatures with increasing field strength for all NBT samples. From Fig. 15b, all the samples showed a positive ECE at higher temperatures. The mixed positive and negative ECE findings are similar to the prior research [64][64]. As a result, the FE to relaxor phase transition is the most effective way to enhance the electro-caloric effect. And the optimum ΔT_{max} near room temperature ~ 30 to 60 °C is the best way for ferroelectric refrigeration applications.

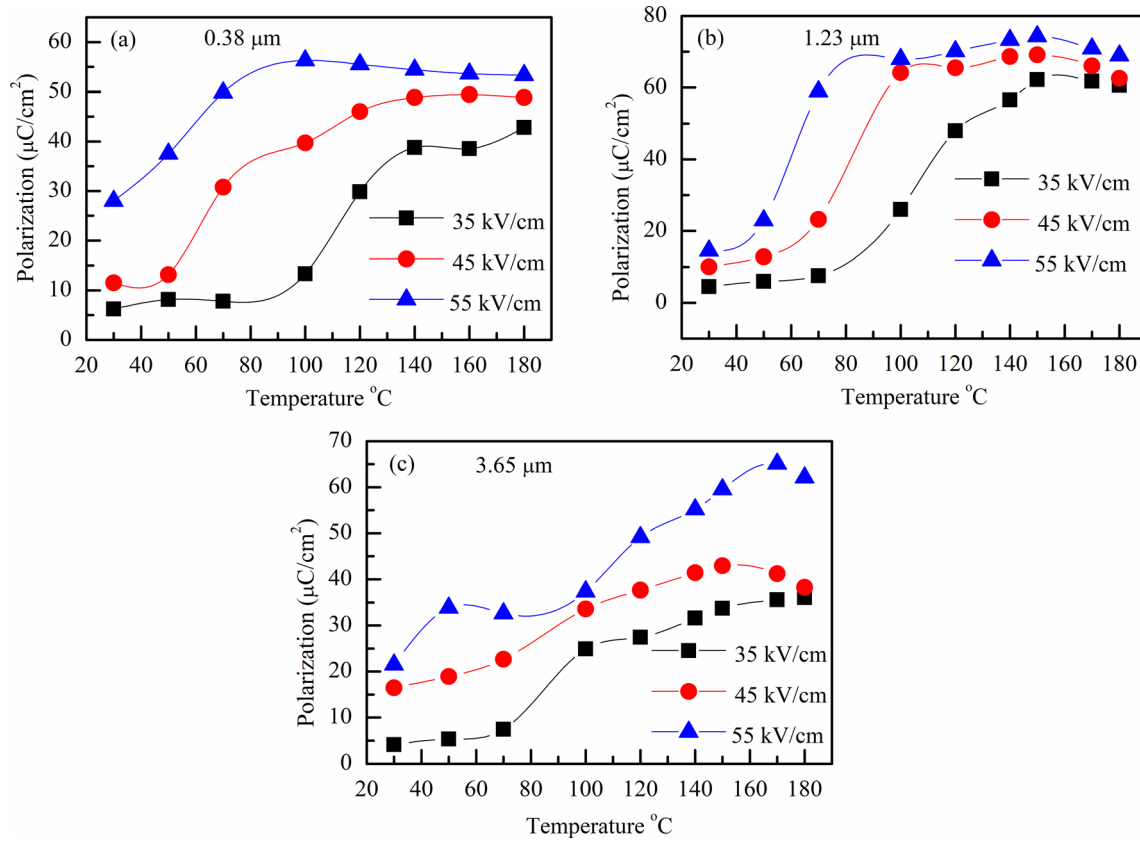


Fig. 14 Temperature vs polarization (P_{max}) graph for a sub-micron b micron c large-micron NBT

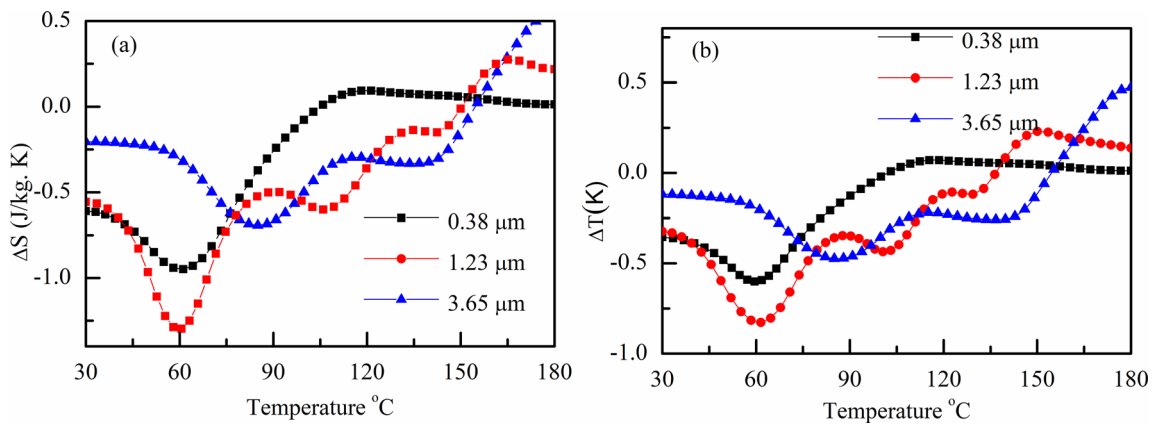


Fig. 15 a Entropy change (ΔS) as the function of temperature (30 to 180 $^{\circ}\text{C}$) for 0.38 μm (sub-micron), 1.23 μm (micron), 3.65 μm (large-micron) b Adiabatic change in temperature (ΔT) as a function of temperature measured at 30 to 180 $^{\circ}\text{C}$ for 0.38 μm (sub-micron), 1.23 μm (micron), and 3.65 μm (large-micron) for field 55 kV/cm

4 Conclusion

In summary, single-phase $\text{Na}_{0.5}\text{Bi}_{0.5}\text{TiO}_3$ (NBT) ceramics with three distinct grains ranging from sub-micron to large-micron were prepared by isothermal sintering with different durations. Rietveld Refinement and Raman analysis confirmed that bulk-NBT was phase pure and structurally stable $R3c$ phase for all the samples. The intrinsic properties like octahedral tilting, octahedral distortions, bond length, bond-angle and lattice parameters have increased with increasing grain growth. The weak superlattice reflection, absence of peak splitting and large lattice strain in XRD along with peak broadening and frequency softening of A-O vibrations in Raman modes all are indicated that the low sintering time results a deflectable sub-micron NBT. It is worth noting that the FE- rhombohedral to AFE-tetragonal phase transition was suppressed in sub-micron NBT due to the impact of uncompensated internal stress which precluded the formation of the tetragonal- 90° domain. The absence of pinched hysteresis from temperature-dependent P–E loop findings shows the suppression of the AFE phase and support for dielectric results. On the other hand, the amount of macroscopic pores increases at a higher sintering time can be related to the decrement in dielectric and ferroelectric properties of large-micron NBT. Finally, a well-saturated perfect ferroelectric loop with enhanced remnant polarization of $P_r \sim 43.12 \mu\text{C}/\text{cm}^2$ and maximum dielectric permittivity of 3016 at high Curie temperature 340°C along with significant electro caloric effect of $\Delta T_{max} = -0.81 \text{ K}$ and large energy storage efficiency of 26.12% ($W_{rec} = 0.55 \text{ J}/\text{cm}^3$) were obtained in micron NBT (1.23 μm) is the optimum size for functional devices.

Acknowledgements

L. Venkidu, one of the authors is acknowledging the UGC-BSR (University Grant Commission-Basic Science Research) scheme provided for the financial support by the UGC -Government of India (F.No:25-1/2014-15(BSR)/7-305/2010/(BSR)). The author also thank Morgane Poupan, Institute of Physics, Czech Academy of Science, Prague, Czech Republic for her valid discussions on Octahedral tilting. Also, a great thank you to Marija Dunce, Institute of Solid State Physics, University of Latvia, Kengaraga 8, Riga LV-

1063, Latvia, for her help in using ImageJ software to analyze porosity.

Author contributions

The corresponding author BS is responsible for ensuring that the descriptions are accurate and agreed by all authors. The role(s) of all authors is listed as follows, LV: Conceptualization, Methodology, Software, Writing—Original Draft DEJR: Validation and Investigation, MVGB: Validation and Investigation, PER: Software, DD: Resource, NVG: Resource, BS: Conceptualization, Methodology, Validation, Investigation, Writing—Review & Editing.

Funding

University Grants Commission, F.No:25-1/2014-15(BSR)/7-305/2010/(BSR)., L Venkidu

Data availability

The datasets generated and analysed during the current study are available from the corresponding author on reasonable request.

Declarations

Conflict of interest The authors declare that they have no known competing financial interests or personal relationships that could have appeared to influence the work reported in this paper.

References

1. M. Sahu, T. Karthik, A. Srinivas, S. Asthana, *J Mater Sci: Mater Electron* **26**, 9741–9746 (2015). <https://doi.org/10.1007/s10854-015-3643-62>
2. Z. Zhao, V. Buscaglia, M. Viviani, M.T. Buscaglia, L. Mitoseriu, A. Testino, M. Nygren, M. Johnsson, P. Nanni, *Phys. Rev. B* **70**, 024107 (2004). <https://doi.org/10.1103/PhysRevB.70.024107>
3. X. Lv, X.-x Zhang, J. Wu, *J. Mater. Chem. A* **8**, 10026–10073 (2020). <https://doi.org/10.1039/D0TA03201H>
4. R. Roy, A. Dutta, *Solid State. Solid State Sci.* **102**, 106174 (2020). <https://doi.org/10.1016/j.solidstatesciences.2020.106174>

5. M.V.G. Babu, B. Bagyalakshmi, L. Venkidu, B. Sundarakannan, *Ceram. Int.* **43**, 12599–12604 (2017). <https://doi.org/10.1016/j.ceramint.2017.06.137>
6. L. Chao, Y. Hou, M. Zheng, Y. Yue, M. Zhu, *Appl. Phys. Lett.* **110**, 122901 (2017). <https://doi.org/10.1063/1.4978904>
7. T.M. Kamel, G. de With, *J. Eur. Ceram. Soc.* **28**, 851–861 (2008). <https://doi.org/10.1016/j.jeurceramsoc.2007.08.010>
8. M. Muthuramalingam, D.E.J. Ruth, M.V.G. Babu, N. Ponpandian, D. Mangalaraj, B. Sundarakannan, *Scripta Mater.* **112**, 58–61 (2016). <https://doi.org/10.1016/j.scriptamat.2015.09.011>
9. A. Verma, A.K. Yadav, N. Khatun, S. Kumar, R. Jangir, V. Srihari, V.R. Reddy, S.W. Liu, S. Biring, S. Sen, *Ceram. Int.* **44**, 20178–20186 (2018). <https://doi.org/10.1016/j.ceramint.2018.07.312>
10. X. Liu, B. Liu, F. Li, P. Li, J. Zhai, B. Shen, *J. Mater. Sci.* **53**, 309–322 (2018). <https://doi.org/10.1007/s10853-017-1517-4>
11. P. Chen, B. Chu, *J. Eur. Ceram. Soc.* **36**, 81–88 (2015). <https://doi.org/10.1016/j.jeurceramsoc.2015.09.029>
12. G. Fan, W. Lu, X. Wang, F. Liang, J. Xiao, *J. Phys. D* **41**, 035403 (2008). <https://doi.org/10.1088/0022-3727/41/3/035403>
13. V. Dorcet, G. Trolliard, P. Boullay, *J. Chem. Mater.* **20**, 5061–5073 (2008). <https://doi.org/10.1021/cm8004634>
14. T. Takenaka, K. Maruyama, K. Sakata, *Jpn. J. Appl. Phys.* **30**, 2236 (1991). <https://doi.org/10.1143/JJAP.30.2236>
15. K. Thangavelu, R. Ramadurai, S. Asthana, *J. Aip Adv.* **4**, 017111 (2014). <https://doi.org/10.1063/1.4862169>
16. G.O. Jones, P.A. Thomas, *Acta Cryst.* **B5**, 168–178 (2002). <https://doi.org/10.1107/S0108768101020845>
17. X.X. Wang, X.G. Tang, H.L.W. Chan, *Appl. Phys. Lett.* **85**, 91 (2004). <https://doi.org/10.1063/1.1767592>
18. S.B. Vakhrushev, V.A. Isupov, B.E. Kvyatkovsky, N.M. Okuneva, I.P. Pronin, G.A. Smolensky, P.P. Syrnikov, *Ferroelectrics* **63**, 153–160 (1985). <https://doi.org/10.1080/00150198508221396>
19. D.K. Khatua, T. Mehrotra, A. Mishra, B. Majumdar, A. Senyshyn, R. Ranjan, *Acta Mater.* **134**, 177–187 (2017). <https://doi.org/10.1016/j.actamat.2017.05.068>
20. Ming-Lei, W. Chun-Lei, Z. Wei-Lie, *Chinese Phys. Lett.* **20**, 290–292 (2003). <https://doi.org/10.1088/0256-307X/20/2/335>
21. M. Duce, E. Birks, M. Antonova, L. Bikse, S. Dutkevica, O. Freimanis, M. Livins, L. Eglite, K. Smits, A. Sternberg, *J. Alloys Compd* **884**, 160955 (2021). <https://doi.org/10.1016/j.jallcom.2021.160955>
22. M.V.G. Babu, B. Bagyalakshmi, B. Sundarakannan, *J Mater Sci.: Mater Electron* **28**, 18620–18629 (2017). <https://doi.org/10.1007/s10854-017-7811-8>
23. M.V.G. Babu, B. Bagyalakshmi, D. PathinettamPadiyan, Y. Ren, B. Sundarakannan, *Scr. Mater.* **141**, 67–71 (2017). <https://doi.org/10.1016/j.scriptamat.2017.07.022>
24. B.K. Barick, K.K. Mishra, A.K. Arora, R.N.P. Choudhary, D.K. Pradhan, *J. Phys. D: Appl. Phys.* **44**, 355402 (2011). <https://doi.org/10.1088/0022-3727/44/35/355402>
25. M. Arshad, W. Khan, M. Abushad, M. Nadeem, S. Husain, A. Ansari, V.K. Chakradhary, *Ceram. Int.* **46**, 27336–27351 (2020). <https://doi.org/10.1016/j.ceramint.2020.07.219>
26. Petříček, Václav, Dušek, Michal, Palatinus, Lukáš, *Zeitschrift für Kristallographie—Cryst. Mater.* **229**(5), 345–352 (2014). <https://doi.org/10.1515/zkri-2014-1737>
27. B.N. Rao, R. Ranjan, *Phys Rev B* **86**, 134103 (2012). <https://doi.org/10.1103/PhysRevB.86.134103>
28. E. Aksel, J.S. Forrester, B. Kowalski, J.L. Jones, P.A. Thomas, *Appl. Phys. Lett.* **99**, 222901 (2011). <https://doi.org/10.1063/1.3664393>
29. L. Qiao, S. Zhang, H.Y. Xiao, D.J. Singh, H.L. Zhang, Z.J. Liu, X.T. Zu, S. Li, *J. Mater. Chem. C* **6**, 1239–1247 (2018). <https://doi.org/10.1039/C7TC04160H>
30. R. Yu, H. Hojo, T. Mizoguchi, M. Azuma, *J. Appl. Phys.* **118**, 094103 (2015). <https://doi.org/10.1063/1.4930034>
31. R. Roukos, N. Zaiter, D. Chaumont, *J Adv Ceram.* **7**, 124–142 (2018). <https://doi.org/10.1007/s40145-018-0264-6>
32. S. Xue, H. Luo, X. Zhao, F. Wang, D. Lin, H. Deng, X. Li, Q. Yue, Y. Tang, B. Fang, H. Zhang, *Scripta Mater.* **165**, 94–97 (2019). <https://doi.org/10.1016/j.scriptamat.2019.02.023>
33. D.E. JainRuth, B. Sundarakannan, *Ceram. Int.* **42**, 4775–4778 (2016). <https://doi.org/10.1016/j.ceramint.2015.11.162>
34. L. Zhang, C. Zhao, T. Zheng, Wu. Jiagang, *ACS Appl. Mater. Interfaces* **12**, 33934–33940 (2020). <https://doi.org/10.1021/acsami.0c09343>
35. J.A. Alonso, M.J. Martínez-Lope, M.T. Casais, *Inorg. Chem.* **39**, 917–923 (2000). <https://doi.org/10.1021/ic990921e>
36. L. Venkidu, A.B. Athanas, S. Kalaiyar, B. Sundarakannan, *Matter. Lett.* **311**, 131473 (2022). <https://doi.org/10.1016/j.mattlet.2021.131473>
37. T. Karthik, D. Radhakrishnan, C. Narayana, S. Asthana, *J. Alloys Compd.* **732**, 945–951 (2018). <https://doi.org/10.1016/j.jallcom.2017.10.126>
38. W. Yang, P. Li, S. Wu, F. Li, B. Shen, J. Zhai, *Adv. Electron. Mater.* **6**, 1900570 (2019). <https://doi.org/10.1002/aeml.201900570>
39. Z. Cai, X. Wang, W. Hong, B. Luo, Q. Zhao, L. Li, *J. Am. Ceram. Soc.* **101**, 5487–5496 (2018). <https://doi.org/10.1111/jace.15803>
40. M.A. Zubair, F.A. Mozahid, H. Takeda, A.K.M.A. Hossain, *Mater. Sci. Eng. B* **274**, 115474 (2021). <https://doi.org/10.1016/j.mseb.2021.115474>

41. K. Gupta, R.M. Quade, B. Gibbons, P. Mardilovich, D.P. Cann, *J. Appl. Phys.* **127**, 074104 (2020). <https://doi.org/10.1063/1.5132536>
42. V.V. Shvartsman, D.C. Lupascu, *J. Am. Ceram. Soc.* **95**, 1–26 (2012). <https://doi.org/10.1111/j.1551-2916.2011.04952.x>
43. R. Dittmer, D. Gobeljic, W. Jo, V.V. Shvartsman, D.C. Lupascu, J.L. Jones, J. Rödel, *J. Appl. Phys.* **115**, 084111 (2014). <https://doi.org/10.1063/1.4867157>
44. Y. Guo, Y. Liu, R.L. Withers, F. Brink, H. Chen, *Chem. Mater.* **23**(2), 219–228 (2011). <https://doi.org/10.1021/cm102719k>
45. A.M. Glazer, *Acta Crystallogr. A* **31**, 756 (1975). <https://doi.org/10.1107/S0567739475001635>
46. M. Hagiwara, S. Fujihara, *Appl. Phys. Lett.* **107**, 012903 (2015). <https://doi.org/10.1063/1.4926496>
47. B.A. Tuttle, T.J. Garino, J.A. Voigt, T.J. Headley, D. Dimos, M.O. Eatough, Relationships between ferroelectric 90° domain formation and electrical properties of chemically prepared Pb(Zr, Ti)O₃ thin films, in *Science and Technology of Electro-ceramic Thin Films*. ed. by O. Auciello, R. Waser (Kluwer, Dordrecht, 1995), p.117
48. M.P. McNeal, S. Jang, R.E. Newnham, *J. Appl. Phys.* **83**, 3288 (1998). <https://doi.org/10.1063/1.367097>
49. M.H. Frey, Z. Xu, P. Han, D.A. Payne, *Ferroelectrics* **206**(1), 337–353 (1998). <https://doi.org/10.1080/00150199808009168>
50. K. Thangavelu, S. Rayapro, V. Siruguri, P.U. Sastry, S. Asthana, *AIP Conf. Proc.* **1665**, 030030 (2015). <https://doi.org/10.1063/1.4917605>
51. J. Li, D. Zhang, S. Qin, T. Li, M. Wu, D. Wang, Y. Bai, X. Lou, *Acta Mater.* **115**, 58–67 (2016). <https://doi.org/10.1016/j.actamat.2016.05.044>
52. S.S. Sundari, B. Kumar, K. Asokan, R. Dhanasekaran, *Appl. Surf. Sci.* **265**, 296–301 (2013). <https://doi.org/10.1016/j.apsusc.2012.10.199>
53. K.R. Kandula, S.S.K. Raavi, S. Asthana, *Ferroelectrics* **518**, 23–30 (2017). <https://doi.org/10.1080/00150193.2017.1360117>
54. M. Algueró, J. Ricote, R. Jiménez, *Appl. Phys. Lett.* **91**, 112905 (2007). <https://doi.org/10.1063/1.2778471>
55. D. Damjanovic, *Rep. Prog. Phys.* **61**, 1267–1324 (1998). <https://doi.org/10.1088/0034-4885/61/9/002>
56. Y. Qin, S. Zhang, Y. Wu, C. Lu, J. Zhang, *J. Eur. Ceram. Soc.* **37**, 3493–3500 (2017). <https://doi.org/10.1016/j.jeurceramsoc.2017.04.047>
57. A. Jain, Y.G. Wang, H. Guo, N. Wang, *J. Am. Ceram. Soc.* (2020). <https://doi.org/10.1111/jace.17346>
58. A. Peláiz-Barranco, F. Calderón-Piñar, O. García-Zaldívar, Y. González-Abreu, Relaxor Behavior in Ferroelectric Ceramics, in *Advances in Ferroelectrics*. ed. by A. PeláizBarranco (InTech, Rijeka, 2012)
59. A. Lakouader, H. Mezzourh, D. Mezzane, M. Amjoud, L. Hajji, E.H. Choukri, I.A.L. Yanchuk, Z. Kutnjak, M.E. Marssi, *J. Mater. Sci.: Mater. Electron.* **33**, 14381–14396 (2022). <https://doi.org/10.1007/s10854-022-08362-y>
60. J. Lv, Q. Li, Y. Li, M. Tang, D. Jin, Y. Yan, B. Fan, L. Jin, G. Liu, *Chem. Eng. J.* **420**, 129900 (2021). <https://doi.org/10.1016/j.ccej.2021.129900>
61. J. Xie, Z. Dai, X. Ding, X. Fan, W. Liu, L. Zhang, J. Li, *J. Mater. Sci.* **55**, 13578–13589 (2020). <https://doi.org/10.1007/s10853-020-04978-9>
62. M. Benyoussef, M. Zannen, J. Belhadi, B. Manoun, Z. Kutnjak, D. Vengust, M. Spreitzer, M.E. Marssi, A. Lahmar, *Ceram. Int* **47**, 26539–26551 (2021). <https://doi.org/10.1016/j.ceramint.2021.06.068>
63. X. Zhang, L. Wu, S. Gao, J.Q. Liu, B. Xu, Y.D. Xia, J. Yin, Z.G. Liu, *AIP Adv.* **5**, 047134 (2015). <https://doi.org/10.1063/1.4919096>
64. X.C. Zheng, G.P. Zheng, Z. Lin et al., Electro-caloric behaviors of lead-free Bi_{0.5}Na_{0.5}TiO₃-BaTiO₃ ceramics. *J. Electroceram.* **28**, 20–26 (2012). <https://doi.org/10.1007/s10832-011-9673-4>
65. Y. Bai, G.-P. Zheng, San-Qiang Shi. *J. Mater. Resear In. Bullet.* **46**, 1866–1869 (2011). <https://doi.org/10.1016/j.materresbull.2011.07.038>

Publisher's Note Springer Nature remains neutral with regard to jurisdictional claims in published maps and institutional affiliations.

Springer Nature or its licensor holds exclusive rights to this article under a publishing agreement with the author(s) or other rightsholder(s); author self-archiving of the accepted manuscript version of this article is solely governed by the terms of such publishing agreement and applicable law.